Journal of Materials Chemistry C

ROYAL SOCIETY OF CHEMISTRY

COMMUNICATION

View Article Online
View Journal | View Issue

Check for updates

Cite this: *J. Mater. Chem. C*, 2025, **13**, 3193

Received 20th November 2024,
Accepted 19th January 2025

DOI: 10.1039/d4tc04911j

rsc.li/materials-c

Wide-bandgap quantum dots with large-span fluorescence switching and two-photon emission *via* protonation/deprotonation†

Yamei Ding,[a] Mingyu Xie,[a] Ping He,[a] Ziqi Zhao,[a] Huiwen Lin[a] and Li Tao *[ab]

Wide-bandgap quantum dots (QDs) have recognized as the third generation of low-dimensional semiconductors with reliable optical response, outstanding stability and biocompatibility for long-term biosensing in health care applications, especially in extreme environments. However, the applicable scenarios are limited, because optical switching over a large span from the wide bandgap (deep UV region) to the visible region is challenging due to the stable framework and the high breakdown difficulty. In this work, we adopted a facile protonation/deprotonation treatment process, which is suitable for different biogenic environments, to modulate the one-photon and two-photon fluorescence of wide-bandgap QDs. Two fluorescent centers are coordinative to control one-photon emission from deep blue (410 nm) to yellow (585 nm) emission with a wide large-span modulation, superior to most reports under different acid–base environments. The electron transition between electron-donating amine ($-NH_2$) groups and H^+ ($-OH$) changes the degree of nonradiative transition, narrowing the breadth of the full width at half maximum (FWHM) by 34.4%. Moreover, our QDs exhibit two-photon fluorescence at 710 nm, which have never reported before for wide-bandgap nitrides. It shows pH-independent two-photon fluorescence because of the intrinsic electron–phonon coupling of the π-conjugated structure. This work introduces a simple design strategy to realize fluorescence control over a large span in wide-bandgap nanomaterials, enabling distensible applications in biological health and pH related linear or nonlinear optical fields.

Introduction

Wide-bandgap semiconductors (WBS) have emerged as a promising candidate in bio-related applications due to their long-term stability, biocompatibility, inoxidizability, and stable electrical and optical properties.[1–4] Compared with conventional organic polymers as flexible carriers, WBS overcome inherent drawbacks such as low electron mobilities and instability in extreme biofluidic environments.[5–7] Inorganic semiconductors such as silicon on soft substrates show better performance in biological tissue, but fast ion diffusion and degradation issues make them unsuitable for long-term implanted devices.[8–10] WBS offset the deficiencies of conventional organic and inorganic materials, with successful attempts in optogenetics, long-lived recording and sensing, and flexible implantable biosensors. However, most WBS are located in the UV region or emit short wavelengths, limiting their applicability in bioenvironmental sensing.[11–13] For instance, the bandgap of boron nitrides (BN) is 5.6 eV, which corresponds to deep UV detection.[12,13] Therefore, adequate functionalization for better and compound performance is desired, because it is extremely challenging to change the intrinsic properties of WBS.

In recent years, the strong quantum confinement and edge effects have resulted in the successful development of two-dimensional (2D) quantum dots (QDs) with unique chemical structures and tunable optical properties in diverse applications.[14–21] Following the antecedent of graphene quantum dots, other 2D semiconductor materials have been stimulated to decompose into zero-dimensional (0D) QDs to achieve the desired performance.[21–25] QDs with various photophysical characteristics, such as tunable photoluminescence (PL), bandgap, broad absorption, emission bandwidth and light excitation responses, have been successfully demonstrated *via* their good tailorability and designability. However, for wide-bandgap QDs, it is difficult to regulate their inherently stable structure and chemical inactivity. Our previous work provides a strategy to prepared multicolor BNQDs *via* the selection of specific amino ligands and solvents to passivate BNQDs for diverse surface states.[26] Other researchers have also adopted similar methods to affect quantum confinement, the edge effect, and surface passivated defects.[27,28] All these methods are tedious and time-consuming, involving an essential chemical process. Thus, it is desirable to explore a facile,

[a] *School of Materials Science and Engineering, Jiangsu Key Laboratory of Advanced Metallic Materials, Southeast University, Nanjing, 211189, China. E-mail: tao@seu.edu.cn*
[b] *Ministry of Education Key Laboratory of Quantum Materials and Devices, Southeast University, Nanjing, 211189, China*

† Electronic supplementary information (ESI) available. See DOI: https://doi.org/10.1039/d4tc04911j

eco-friendly, and cost-effective method to modulate wide-bandgap materials with accessible optical switching and response under variable environments.

Herein, we present wide-bandgap QDs based on boron nitride (BN) with long-span fluorescence switching from deep-blue (410 nm) to yellow (585 nm) emission *via* simple protonation–deprotonation treatment. This wide switching results from the two PL peaks of the QDs, which cover the visible region. The full width at half maximum (FWHM) is made 34.4% narrower, being reduced to 80 nm. Up-conversion fluorescence of BNQDs has also been achieved, demonstrating two-photon absorption behaviors. Our work provides a simple strategy to control and analyze the one-photon and two-photon luminescence properties of BNQDs in different pH environments for a broad range of bio-applications.

Experimental section

Materials

Hexagonal boron nitride (h-BN, ≥99.9%), methylbenzene (≥99.5%), and *p*-phenylenediamine (PPD, ≥97.0%) were purchased from Aladdin Industrial Corporation. Ethanol (≥95.0%) and hydrochloric acid (36.0–38.0%) were purchased from Sinopharm Group Chemical Practice company. Sodium hydroxide (≥96.0%) was purchased from Meryer. Deionized water was obtained from a water purification machine. PTFE membranes (220 nm) were products of Jin Teng. The pH meter was purchased from SMSART SENPR.

Preparation of BNQDs

First, 0.5 g BN powder was crushed using an ultrasonic crusher in ethanol solvent for 10 min. Subsequently, 5 mL of the supernatant BNNSs was taken after quiescence for 24 h and dried into a polytetrafluoroethylene Teflon-lined autoclave. Then, 0.05 g PPD and 15 mL methylbenzene were added to mix together. The autoclave was then heated at 200 °C for 10 h and cooled to room temperature naturally. The obtained product was purified by filtration with a 220-nm PTFE membrane.

pH modulation

Initially, 1 mL of the stock solution was taken and diluted with 5 mL of the solvent methylbenzene. Then, 40 g sodium hydroxide was added to 40 mL DI water and stirred magnetically until completely dissolved. Hydrochloric acid or sodium hydroxide solution was added drop-by-drop to the BNQDs, and the pH was monitored using a pH meter.

Contrast experiment

In brief, 0.5 g BN powder was crushed using the ultrasonic crusher in ethanol for 10 min. Five milliliters of the supernatant BNNSs was taken after quiescence for 24 h and dried in a polytetrafluoroethylene Teflon-lined autoclave. Then, 0.05 g PPD and 15 mL methylbenzene were added to mix together. Hydrochloric acid or sodium hydroxide solution was added to the precursor solutions to achieve pH 2 and 13, as monitored using a pH meter. The autoclave was heated at 200 °C for 10 h and cooled to room temperature naturally. The obtained product was purified by filtration with a 220-nm PTFE membrane.

Characterization

The structural test was aided by transmission electron microscope (Tecnai G20, FEI) and high-resolution transmission electron microscope (Tecnai G20, FEI) characterizations. Photoluminescence was characterized using a fluorescence spectrometer (F-7000, Nichia), and absorption spectra were measured using an ultraviolet spectrophotometer (UV-2600, Shimadzu). Fourier transform infrared spectroscopy (Nicolet iS10, Thermo Scientific) spectra were measured neat on a KBr plate. Zeta potentials were tested using a JS94H micro electrophoresis instrument. The quantum yield (QY) was measured using a fluorescent life test system (FLS 1000, Edinburgh). Up-conversion PL was measured using an 808-nm laser with the Edinburgh system.

Results and discussion

pH-Dependent one-photon fluorescence

Wide-bandgap BN was selected as the precursor to synthesize BNQDs in a colloidal solution *via* a high-power ultrasound and eco-friendly hydrothermal method. In detail, the BN precursor was obtained as uniform nanosheets using an ultrasonic crusher (Fig. S1, ESI†) and then subjected to a hydrothermal reaction, passivating it with PPD. Compared with pristine BNQDs with pH-independent blue emission (Fig. S2, ESI†), the functionalized BNQDs emit two main luminescence peaks at around 470 and 585 nm, corresponding to the blue and yellow light region, which cover the visible region (Fig. 1a). The PL properties demonstrate pH-dependent fluorescence behavior. The intensity of blue peak is enhanced, while the yellow peak is weakened, as the pH value is increased from 2 to 13. Optical images of the QDs varied from yellow, to green, white, blue and deep blue emission under 365-nm irradiation (Fig. 1b and Fig. S3, ESI†). Among these, we chose three pH values, 2, 7, and 13 for further detailed study.

Optical properties of the two fluorescence peaks

The two fluorescence peaks of the QDs exhibit excitation-dependent and excitation-independent behavior when excited by excitation wavelengths varying from 320 to 520 nm. At pH 2, the intensity of blue peaks declines and they exhibit a gradual red-shift, with yellow emission dominating (Fig. 1c and Fig. S4a, ESI†). Under neutral conditions, the QDs feature white emission with appropriate intensity proportions of the blue and yellow centers (Fig. 1d and Fig. S4b, ESI†). At pH 13, the blue peak outcompetes the yellow one, blue-shifting from 470 to 410 nm, resulting in deep blue emission (Fig. 1e and Fig. S4c, ESI†). Compared with the reported pH-controlled QDs in Table 1, the change in the emission position shows a wider span, from 410 to 585 nm.[29–33] This is attributed to the coordination of the two emerging fluorescence centers covering the visible region *via* a protonation and deprotonation process.

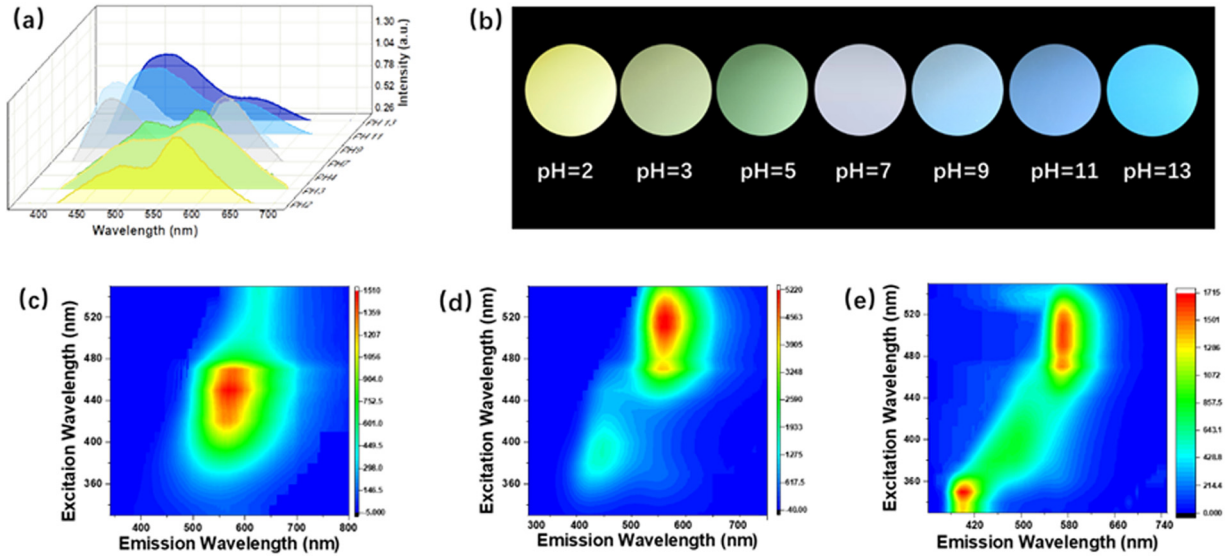

Fig. 1 Optical performance of the BNQDs at different pH values from 2 to 13. (a) and (b) PL spectra and corresponding optical images of the QDs at pH values from 2 to 13 under 365-nm irradiation. Normalized 3D FL spectra under different irradiation wavelengths at pH 2 (c), 7 (d), and 13 (e).

To explore the effect of the surface functional groups on the two fluorescence peaks of the QDs, their PL decay and UV-vis absorption are illustrated in Fig. 2. The fluorescence decay curve can be fitted by a two-exponential function corresponding to recombination from the intrinsic state (τ_1) and surface state (τ_2), respectively (Fig. 2a–c).[32] The acid–base environment did not affect the intrinsic structure of the quantum dots due to the stable frame of the skeleton; thus, τ_1 is steady (Table S1, ESI†). However, the surface groups are sensitive, as confirmed by the decreased lifetime of the surface states (τ_2). This result is further demonstrated by UV-vis absorption in Fig. 2d–f. The absorption band of the UV light region observed at 320 nm results from the $\pi \rightarrow \pi^*$ transition of the conjugated structure of BN, and the visible light absorption is blue-shifted from 520 to 380 nm, caused by the sensitive $n \rightarrow \pi^*$ transition of the changed surface groups. These observations reveal that the core skeleton of the BNQDs exhibits stable behavior during the protonation and deprotonation process, while the surface states are highly sensitive to different pH values, which may dominate the electron transition process of the surface groups. We demonstrated a contrast experiment *via* pH modulation of the precursor before hydrothermal reaction. Different particle sizes were observed in the TEM images, while just one fluorescence peak was located in the blue region, similar to the pristine BNQDs (Fig. S5 and S6, ESI†). This indicates that acid–base treatment before the hydrothermal reaction terminates the amidation process of the QDs, but cannot affect the core formation of the BNQDs. Thus, the variable emission characteristics of BNQDs result from their pH-sensitive surface states through suitable passivation, rather than the sizes.

Table 1 Comparison of different pH-modulated quantum dots

Quantum dot	Peaks	pH value	Emission	Ref.
Carbon	One	1–13	~430–460 nm	29
Carbon	One	1–14	550–620 nm	30
MoS_2	One	1–13	375–441 nm	31
$MoSe_2$	One	2–11	~450–470 nm	32
B–carbon	One	3–13	435–508 nm	33
BN	**Two**	**2–13**	**410–585 nm**	**This work**

Particle morphology and structure

Transmission electron microscopy (TEM) images demonstrate that the particle size of BNQDs ranges from 1 to 4 nm with an average dimension of 2.2 nm (Fig. 3a–c). It has been reported that for QDs, there is a red-shift of the PL as the size decreases. However, in our case, the size of the QDs is independent of the variation in the emission due to the intrinsic stability of the precursors. High-resolution images show that the QDs have a lattice distance of 0.22 nm, attributed to the (1, 1, 0) plane of BN (Fig. 3d–f). The particle size distribution (Fig. 3g–i) was fitted by a Gaussian function without obvious agglomeration, even in strong acid and base.

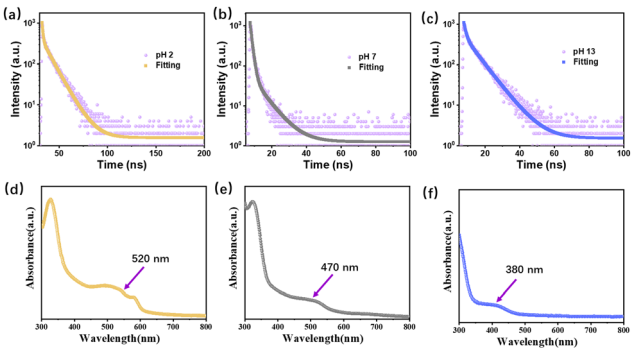

Fig. 2 Electron-transition-related optical properties at different pH values. The decay spectra (a)–(c) and UV-vis absorption (d)–(f) of BNQDs under different pH values.

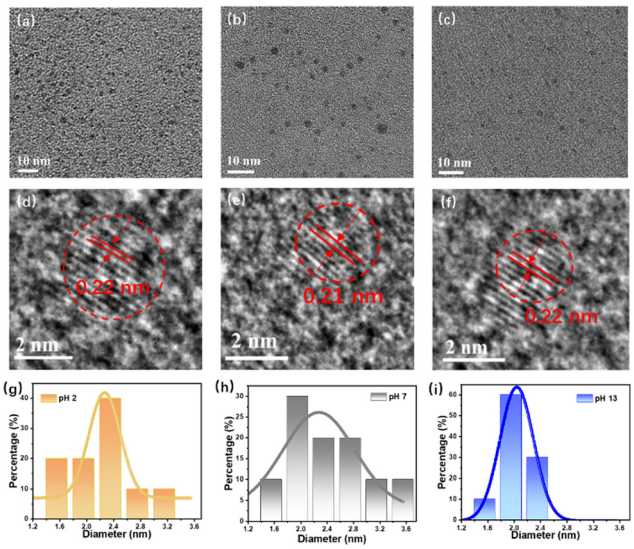

Fig. 3 Structural characterization. TEM images (a)–(c) and corresponding HRTEM images (d)–(f) of the QDs at pH 2, 7, and 13. (g)–(i) Particle distribution of QDs at different pH values.

To identify the intrinsic cause of the change in the fluorophores, the surface functional group species on the QDs were analyzed using Fourier transform infrared spectroscopy (FTIR) and Zeta potential. As shown in Fig. 4a, the characteristic peaks of BN are located at around 1400 cm^{-1}. During the protonation treatment, an $-NH_2$ vibration at around 3200 cm^{-1} emerges, and the bending vibration of the $-NH_2$ amino groups at around 1600 cm^{-1} is red-shifted due to the absorbed H^+ ion. In the deprotonation process, the –OH stretching vibration between 3400 and 3500 cm^{-1} is increased. These changes are verified by the Zeta potential measurements shown in Fig. 4b, which are valid evidence for the protonation and deprotonation process. A well-pronounced linear relationship (R_2 = 0.98) between the Zeta-potential and pH values further demonstrated pH-dependent PL behavior. The surface potential of the QDs increased from −14.98 to 8.48 mV after acidic treatment, while they decreased to −35.05 mV after alkali treatment. In addition to the colored PL, the FWHM narrows by 34.4% from 122 to 80 nm as the pH value increases. The surface fluorophore strongly affects the molecular state of the quantum dots, leading to enhanced dipole–dipole coupling, thus narrowing the FWHM (Fig. 4c) and changing the QY as well (Table S2, ESI†).

Therefore, the relationship between functional groups and optical switching *via* pH control is exhibited in Fig. 4d. The PL of the BNQDs is composed of blue and yellow peaks from the passivated $-NH_2$ functional fluorophores and BN band-edge emission from amidation, respectively. The surface states can be easily affected by the solvent environment. Under acidic conditions, dipole–dipole coupling ($-NH_3^+$) is formed from the interaction between the H^+ ion and $-NH_2$ groups, leading to the decrease in the blue peaks. Under alkali conditions, the $-NH_2$ groups absorb carboxyl groups (–OH) for more electronegative alkaline groups.

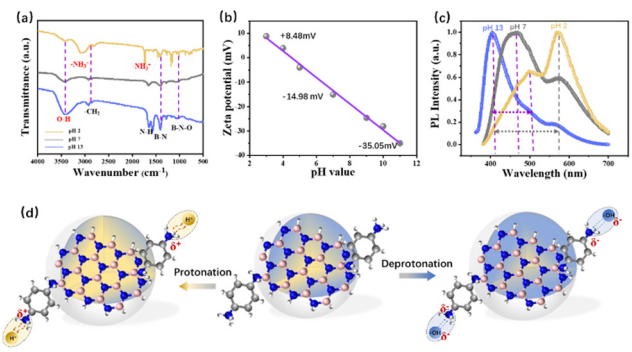

Fig. 4 Changes in FWHM, potential and functional groups under protonation and deprotonation. (a) FTIR spectra, (b) Zeta potential and (c) FWHM of the BNQDs at different pH values. (d) Schematic diagram of the relationship between functional groups and PL switching.

pH-Independent two-photon fluorescence

The two-photon fluorescence properties of the BNQDs were first evaluated and excited using a near-infrared (NIR) 808-nm laser, as shown in Fig. 5. The up-conversion emission is located at 720 nm under different pulsed infrared laser excitation powers (Fig. 5a). The FL intensity increases according to a linear relationship (R = 1.003) as the square of laser power increases from 0.3 to 7.5 W (Fig. 5b). This indicates that the red up-conversion photoluminescence of QDs corresponds to two-photon absorption behavior.[34] Unlike the one-photon properties, the emission wavelength and FWHM show pH-independent behavior, with just the intensity decreasing with increased pH (Fig. 5c and d). The pristine and contrast BNQDs still show two-photon fluorescence at 720 nm with weak intensity (Fig. S7, ESI†). This indicates that the two-photon PL is not controlled by the surface states. Actually, the two-photon PL originates from a virtual energy level between the primitive ground state and excited state for excited state absorption (ESA), which is assisted by phonon coupling.[35] This intrinsic

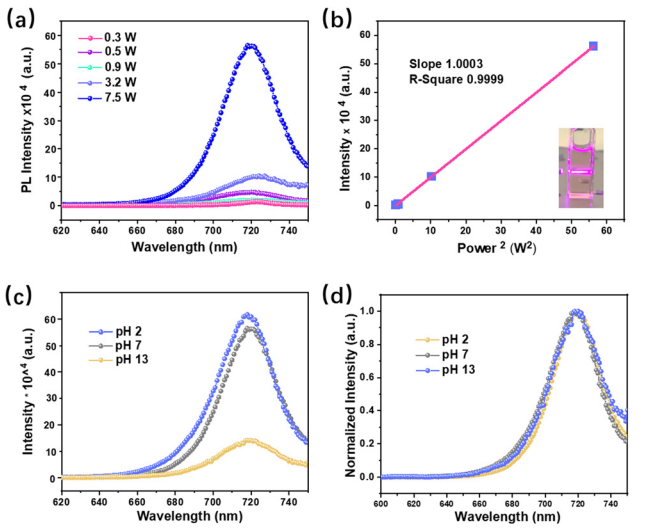

Fig. 5 Two-photon PL of QDs under 808-nm laser. (a) Two-photon spectra with different laser excitation intensities at 808 nm. (b) Relationship between the two-photon emission intensity and the square of laser power. Two-photon spectra (c) and normalized spectra (d) at different pH values.

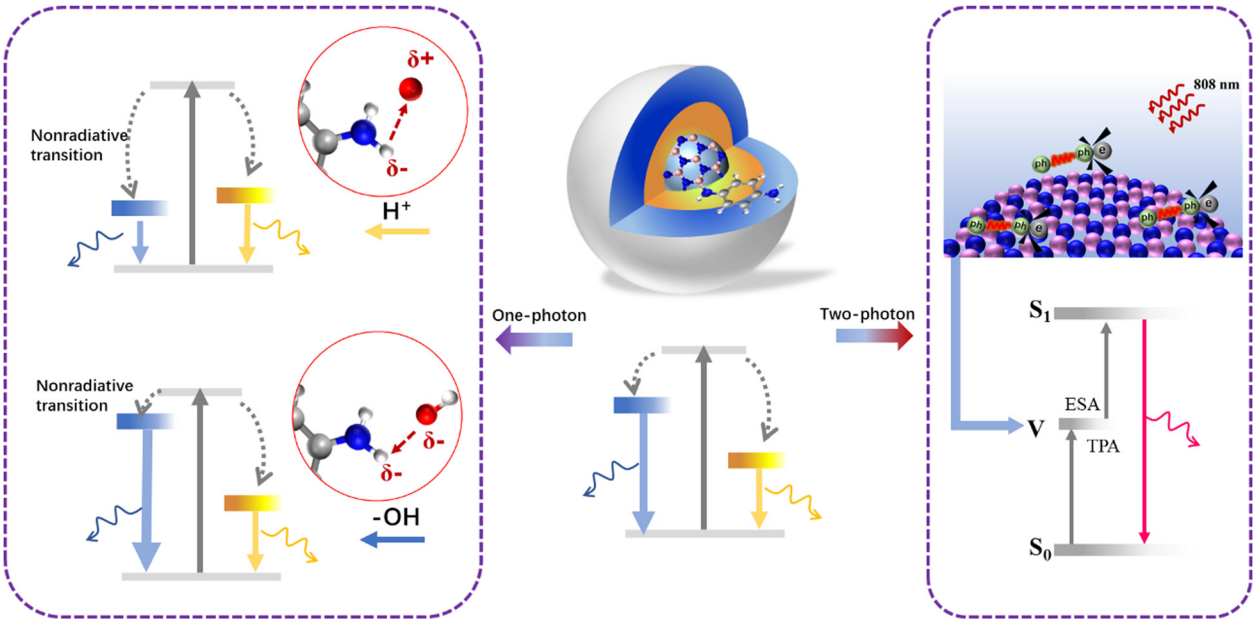

Fig. 6 Changes in the charge transitions of the QDs by protonation and deprotonation treatment.

process is closely related to electron transition between π-conjugated BN, and thus less affected by pH.

Mechanism of protonation/deprotonation process

One-photon and two-photon luminescence are two kinds of distinct Stokes and anti-Stokes processes; thus, PL evolution under different pH values is diverse. Fig. 6 presents the mechanism of the internal energy level variation of the QDs through the protonation and deprotonation treatment. As-prepared BNQDs are composed of blue and yellow photoluminescence peaks, corresponding to $-NH_2$ fluorophores and passivating amidation. The surface $-NH_2$ groups are sensitive to H^+ attack to form $-NH_3^+$ dipole–dipole coupling, leading to increased nonradiative transition. As a result, the blue peak gives way to the yellow one with a relatively weak contribution of the blue portion. Under alkaline conditions, the deprotonation process reduces the nonradiative recombination with dominant blue emission. Therefore, the QDs under different pH values exhibit different colours from deep blue to yellow emission. Nevertheless, up-conversion luminescence results from intrinsic electron–phonon coupling between π-conjugated BN with ESA from a virtual level. Combined with the results from the fluorophore structure analysis, it can be concluded that the protonation and deprotonation process changes the surface states of the QDs, thus controlling the surface-state-triggered one-photon PL, but it is difficult to change the internal π-conjugated BN framework, which is related to the two-photon luminescence.

Conclusions

In summary, we have provided a facile approach to synthesize and modulate wide-bandgap QDs featuring one-photon PL emission with tunable emission from the deep blue (410 nm) to yellow (585 nm) region and NIR-induced two-photon red FL emission at 720 nm. This wide long-span regulation of the emission results from the changeable intensity and position of the blue and yellow fluorescence peaks of the BNQDs due to different degrees of nonradiative transition *via* protonation and deprotonation treatment. The dipole–dipole coupling effect narrows the width of the FWHM by 34.4% and triggers changes in the QY. Moreover, up-conversion luminescence at 720 nm under NIR irradiation of 808 nm can be observed with two-photon absorption features, and is guided by intrinsic electron–phonon coupling from π-conjugated BN. Our results provide a reliable way to realize wide large-span fluorescence switching and up-conversion emission in wide-bandgap semiconductors for a broad range of bio-applications.

Author contributions

Y. D.: investigation, data analysis and writing original draft; M. X.: experiment and data analysis; P. H.: experiment; Z. Z.: experiment; H. L.: investigation and data analysis; L. T. methodology and writing review. All authors gave final approval for publication and agreed to be held accountable for the work performed therein.

Data availability

Further data supporting this article have been included as part of the ESI.†

Conflicts of interest

There are no conflicts to declare.

Acknowledgements

This work was supported by the National Key R&D Program of China (2022YFB4400100), the National Natural Science Foundation of China (92164102, T2321002, and 61725402), and the Jiangsu Province Key R&D Program (BE2023009-3).

References

1 J. H. Kang, M. Ebaid, D. K. Jeong, J. K. Lee and S. W. Ryu, *J. Mater. Chem. C*, 2016, **4**, 3337–3341.
2 S. J. Pearton, D. P. Norton and F. Ren, *Small*, 2007, **3**(7), 1144–1150.
3 T. A. Pham, T. K. Nguyen, R. K. Vadivelu, T. Dinh, A. Qamar, S. Yadav, Y. Yamauchi, J. A. Rogers, N. T. Nguyen and H. P. Phan, *Adv. Funct. Mater.*, 2020, **30**(43), 2004655.
4 J. Rodrigues, S. O. Pereira, J. Zanoni, C. Rodrigues, M. Bras, F. M. Costa and T. Monteiro, *Chemosensors*, 2022, **10**(2), 39.
5 G. Schwartz, B. C. K. Tee, J. G. Mei, A. L. Appleton, D. H. Kim, H. L. Wang and Z. N. Bao, *Nat. Commun.*, 2013, **4**, 1859.
6 K. Kawano, R. Pacios, D. Poplavskyy, J. Nelson, D. D. C. Bradley and J. R. Durrant, *Sol. Energy Mater. Sol. Cells*, 2006, **90**(20), 3520–3530.
7 Y. Yu, X. Wu and J. Wan, *Sci. Sin., Chem.*, 2016, **46**(7), 643–655.
8 D. H. Kim, N. Lu, R. Ghaffari and J. A. Rogers, *NPG Asia Mater.*, 2012, **4**, e15.
9 Y. Sun and J. A. Rogers, *Adv. Mater.*, 2007, **19**(15), 1897–1916.
10 J. Millan, P. Godignon, X. Perpina, A. Perez-Tomas and J. Rebollo, *Ieee Trans. Power Electron.*, 2014, **29**(5), 2155–2163.
11 S. Fujita, *Jpn. Appl. Phys.*, 2015, **54**, 3.
12 X. Y. Liu, C. X. Shan, H. Zhu, B. H. Li, M. M. Jiang, S. F. Yu and D. Z. Shen, *Sci. Rep.*, 2015, **5**, 13641.
13 S. Mitra, Y. Pak, N. Alaal, M. N. Hedhili, D. R. Almalawi, N. Alwadai, K. Loganathan, Y. Kumarasan, N. Lim, G. Y. Jung and I. S. Roqan, *Adv. Opt. Mater.*, 2019, **7**(21), 1900801.
14 D. D. Deepesh Gopalakrishnan and M. M. Shaijumon, *ACS Nano*, 2014, **8**(8), 5297–5303.
15 S. T. Han, L. Hu, X. Wang, Y. Zhou, Y. J. Zeng, S. Ruan, C. Pan and Z. Peng, *Adv. Sci.*, 2017, **4**(8), 1600435.
16 H. Lin, C. Wang, J. Wu and Z. Xu, *New J. Chem.*, 2015, **39**(11), 8492–8497.
17 S. Liu, S. Lin, P. You, C. Surya, S. P. Lau and F. Yan, *Angew. Chem., Int. Ed.*, 2017, **56**(44), 13717–13721.
18 X. Zhang, H. Wang, H. Wang, Q. Zhang, J. Xie, Y. Tian, J. Wang and Y. Xie, *Adv. Mater.*, 2014, **26**(26), 4438–4443.
19 Q. Xue, H. Zhang, M. Zhu, Z. Pei, H. Li, Z. Wang, Y. Huang, Y. Huang, Q. Deng, J. Zhou, S. Du, Q. Huang and C. Zhi, *Adv. Mater.*, 2017, **29**, 15.
20 X. Wang, G. Sun, N. Li and P. Chen, *Chem. Soc. Rev.*, 2016, **45**(8), 2239–2262.
21 H. S. Jin, D. H. Kim, G. H. Jun, S. H. Hong and S. Jeon, *ACS Nano*, 2013, **7**, 1239–1245.
22 B. Sapkota, A. Benabbas, H. G. Lin, W. Liang, P. Champion and M. Wanunu, *ACS Appl. Mater. Interfaces*, 2017, **9**(11), 9378–9387.
23 H. Levy-Falk, O. Capelle, T. Liu, D. Medina-Lopez, E. Deleporte, S. Campidelli, L. Rondin and J. S. Lauret, *Phys. Status Solidi B*, 2023, **260**(12), 2370033.
24 L. J. Wang, G. Cao, T. Tu, H. O. Li, C. Zhou, X. J. Hao, G. C. Guo and G. P. Guo, *Chin. Phys. Lett.*, 2011, **28**(6), 067301.
25 J. Zhu, Y. Tang, G. Wang, J. Mao, Z. Liu, T. Sun, M. Wang, D. Chen, Y. Yang, J. Li, Y. Deng and S. Yang, *ACS Appl. Mater. Interfaces*, 2017, **9**(16), 14470–14477.
26 Y. Ding, P. He, S. Li, B. Chang, S. Zhang, Z. Wang, J. Chen, J. Yu, S. Wu, H. Zeng and L. Tao, *ACS Nano*, 2021, **15**(9), 14610–14617.
27 Z. Lei, S. Xu, J. Wan and P. Wu, *Nanoscale*, 2015, **7**(45), 18902–18907.
28 H. Li, R. Y. Tay, S. H. Tsang, X. Zhen and E. H. Teo, *Small*, 2015, **11**(48), 6491–6499.
29 X. Fan, Y. Wang, B. Li, C. Shen, Z. Sun, Y. Zhan and Y. Zhang, *Nanotechnology*, 2022, **33**(26), 265002.
30 Q. Zhang, R. Wang, B. Feng, X. Zhong and K. Ostrikov, *Nat. Commun.*, 2021, **12**(1), 6856.
31 H. Mishra, S. Umrao, J. Singh, R. K. Srivastava, R. Ali, A. Misra and A. Srivastava, *Adv. Opt. Mater.*, 2017, **5**(9), 1601021.
32 B. Ko, J. Ahn and S. H. Song, *Materials*, 2022, **15**(14), 4945.
33 O. Ustun, S. N. Karadag, H. Mazlumoglu, A. Yilmaz and M. Yilmaz, *Coatings*, 2023, **13**(2), 456.
34 S. Lu, L. Sui, Y. Liu, X. Yong, G. Xiao, K. Yuan, Z. Liu, B. Liu, B. Zou and B. Yang, *Adv. Sci.*, 2019, **6**(9), 1801470.
35 J. Zhou, Q. Liu, W. Feng, Y. Sun and F. Li, *Chem. Rev.*, 2015, **115**(1), 395–465.

